buildings

MDPI

Article

Microstructure and Phase Characterization of Alkali-Activated Slag–Fly Ash Materials with Tetrasodium of 1-Hydroxy Ethylidene-1, 1-Diphosphonic Acid (HEDP·4Na)

Bo Zhou [1,2], Mingyang Zhang [3], Jiaqing Zhang [2] and Jingjie Wei [4,*]

[1] Department of Civil Construction and Environmental Engineering, Iowa State University, Ames, IA 50010, USA; bozhou@iastate.edu
[2] Guangdong Provincial Key Laboratory of Durability for Marine Civil Engineering, College of Civil and Transportation Engineering, Shenzhen University, Shenzhen 518060, China; zjq10011001@gmail.com
[3] College of Civil and Transportation Engineering, Shenzhen University, Shenzhen 518060, China; zhang601@szu.edu.cn
[4] Department of Civil, Architectural and Environmental Engineering, Missouri University of Science and Technology, Rolla, MO 65401, USA
* Correspondence: jwxhc@mst.edu

Abstract: The effect of tetrasodium of 1-hydroxy ethylidene-1, 1-diphosphonic acid (HEDP·4Na) on the microstructure and phase characterization of alkali-activated fly ash–slag (AAFS) materials is not clear or well documented. In this study, XRD, DTG, TAM-air, and SEM analyses of AAFS were used to identify the microstructural changes in AAFS made with HEDP·4Na. Meanwhile, the workability and compressive strength of AAFS were evaluated. The results demonstrated that the early-age alkaline-activated reactions were retarded due to the addition of HEDP·4Na in the AAFS mixture. However, the degree of gel formation was relatively increased at a later age in the AAFS made with HEDP·4Na compared to the plain AAFS mixture. Additionally, in comparison to the control group, the incorporation of HEDP·4Na in AAFS specimens resulted in improved flowability, with increments of 5%, 15%, and 24% for concentrations of 0.1%, 0.2%, and 0.3%, respectively. The initial and final setting times were prolonged by 5% to 50%, indicating a beneficial impact on the rheological properties of the AAFS fresh mixture. Furthermore, the addition of HEDP·4Na led to an improvement in compressive strength in the AAFS mixtures, with enhancements ranging from 13% to 16% at 28 days compared to the control group. With the presence of HEDP·4Na, the increase in the degree of reactions shifted to the formation of gel phases, like C-S-H, through the combined measurement of TGA, XRD, and SEM, resulting in a denser microstructure in the AAFS matrix. This study presents novel insights into the intricate compatibility between the properties of AAFS mixtures and HEDP·4Na, facilitating a more profound comprehension of the potential improvements in the sustainable development of AAFS systems.

Keywords: AAFS; microstructure; workability; compressive strength; HEDP·4Na

check for updates

Citation: Zhou, B.; Zhang, M.; Zhang, J.; Wei, J. Microstructure and Phase Characterization of Alkali-Activated Slag–Fly Ash Materials with Tetrasodium of 1-Hydroxy Ethylidene-1, 1-Diphosphonic Acid (HEDP·4Na). *Buildings* **2024**, *14*, 1383. https://doi.org/10.3390/buildings14051383

Academic Editor: Mizan Ahmed

Received: 5 April 2024
Revised: 26 April 2024
Accepted: 9 May 2024
Published: 12 May 2024

1. Introduction

Alkali-activated materials (AAMs), which utilize industrial by-products such as fly ash (FA), slag, or metakaolin, are recognized as a sustainable low-carbon alternative to traditional Portland cementitious materials (PCMs). These alternatives are noted for the reduction in carbon dioxide emission and energy consumption, as well as minimal exploitation of natural resources [1–5]. For example, the life cycle assessment (LCA) of alkali-activated mortars conducted by Gopalakrishna and Dinakar [6] revealed significantly lower Embodied Energy (EE) and Global Warming Potential (GWP) values compared to mortar made with PCMs. The reductions in EE and GWP were as much as 94% and 97%, respectively. Although numerous investigations regarding AAMs are well documented,

significant challenges need to be addressed to enhance their application within the industry. For example, alkali-activated slag (AAS) shows poor workability because of the large viscosity of the fresh mixes and quick setting [2,7,8], while alkali-activated fly ash (AAF) often struggles to achieve the required strength at an early age owing to the low chemical activity of FA [9–11].

To address the previously mentioned challenge, recent investigations into alkali-activated materials (AAMs) have increasingly concentrated on the hybrid of AAF and AAS, known as AAFS. This hybrid system comprises components of crystalline and amorphous phases at the microstructural level, including N-A-S-H, N-C-A-S-H, and C-A-S-H gels within the AAFS system (CaO-SiO_2-Al_2O_3), each with varying degrees of cross-linking [12,13]. The formation of these hydration products plays a crucial role in the microstructure evolution within the AAFS matrix, potentially involving the development of AAFS mechanical performances. Furthermore, more than 90% of the binder weight is taken up by these three types of reaction products in the AAFS paste [14]. Leveraging the complementary synergistic properties of AAF and AAS, AAFS has shown improvements in engineering performance, such as shrinkage, freezing and thawing resistance, compressive strength, and flexural strength [2,15–17]. For instance, Vigneshkumar et al. [18] investigated the effects of FA- and GGBS-based Self-Compacting Geopolymer Concrete (SCGC) with sodium silicate and sodium hydroxide solutions as activators on fresh and mechanical properties. Their research revealed that incorporating a combination of 50% GGBS and 50% FA by weight resulted in significant enhancements in compressive strength (32.95% and 32.68%), flexural strength (38.92% and 61.81%), and split tensile strength (18.40% and 49.53%) at 28 days, compared to SCGC formulations based solely on FA or GGBS. Li et al. [19] utilized phosphoric acid as an activator with high-magnesium nickel slag (HMNS) and FA to prepare geopolymers, resulting in the production of HMNS-FA-phosphate-based geopolymers with superior mechanical properties. Bayraktar et al. [20] explored the use of different recycled sands in the production of a sustainable one-part alkali-activated slurry-infiltrated fiber concrete or composite made with slag and FA. The authors identified the ideal AAFS mixtures that resulted in higher compressive strengths, freeze–thaw resistance, flexural toughness, and high-temperature resistance. The study highlighted the potential of these materials for construction applications, especially in times of natural sand shortages [19–22]. In summary, compared to AAS or AAF, the micro- and macroscopic performance improvement of AAFS depends on the dissolution of FA and slag particles and the subsequent formation of binding gels (N-A-S-H, N-C-A-S-H, and C-A-S-H gels), as indicated in [2,23]. Therefore, the dissolution behavior of FA and slag particles in AAFS is critical to forming a durable and integral matrix [24,25].

While AAFS demonstrates superior engineering performance over AAF or AAS, its fresh performance requires further enhancement before widespread industry adoption, facilitating transportation, pumping, and integration into the construction process [26]. Chemical admixtures play a vital role in modern high-performance concrete mix proportion design. Extensive research has focused on the influence of different chemical admixtures on the properties of AAFS. Superplasticizers (SPs) based on naphthalene and polycarboxylate ether are recognized as effective performance enhancers, improving workability for AAFS when activated with SH and SS solutions [27–29]. However, such SPs can influence the dissolution behavior of FA and slag, potentially impacting the strength of AAMs [27,30,31]. Another essential admixture is retarders, such as organic phosphonates ($C_{10}H_{12}N_2Na_4O_8 \cdot 4H_2O$, EDTA-4Na) [32]. These phosphonates exhibit biodegradability and compatibility with the environment, and conform to regulatory guidelines by forming stable complexes with metal ions [33,34]. However, the cost and efficiency of delaying setting depend on the type of retarder [32].

Tetrasodium salt of 1-hydroxyethylidene-1,1-diphosphonic acid (HEDP·4Na) serves as a widely used metal corrosion inhibitor in various industrial applications, including chemical and metallurgical water treatments [35]. It has the capability to dissolve different metal oxides and form stable complexes. The use of HEDP·4Na in Portland, magnesium

oxysulfate, and oil well cement has been verified as an effective retarder, and exhibits good efficiency in delaying the setting time of PCMs [5,36–38]. For instance, Ramachandran et al. [5] demonstrated that the addition of HEDP·4Na to Portland cement extended the induction period from about 3 h to over 72 h, indicating its superiority over other concrete additives. The study conducted in [37] also suggested that using HEDP influenced the hydration kinetics and setting behavior of Portland cement pastes. Furthermore, Lupu et al. [38] elucidated the reaction mechanism between $CaCO_3$ and hydration-retarding phosphonate inhibitor agents in a cement matrix by using vertical scanning interferometry (VSI) and X-ray photoelectron spectroscopy (XPS) techniques. For instance, the hydration process and setting time of cement pastes were extended due to these kinds of phosphonates, like ATMP, HEDP, HEDP·4Na, and DTPMP [32,34]. This is because these compounds possess strong chelating or complexing capability, which can potentially poison CH and C-S-H nucleation. As a result, the formation of a metastable C-S-H film on the surface of cementitious material grains delays the progress of the hydration reaction. Additionally, these organic phosphonates also help to retard the setting time in the AAS system [39,40]. Wei et al. [22] reported that the addition of 0.3% and 0.6% HEDP·4Na to fiber-reinforced alkali-activated slag composites (FR-AASC) prolonged the initial and final setting times by 33% and 60%, and 54% and 31%, respectively, compared to the control group. This study showed that the presence of HEDP·4Na significantly delayed the setting time of FR-AASC. However, there are limited studies regarding the effect of HEDP·4Na on the performance of AAFS, especially regarding changes in microstructure and phase characteristics, as these are essential to understand the mechanism of the retarding effect in the AAFS system.

Based on the aforementioned review, this study aims to explore the impact of HEDP·4Na on the fresh performance and setting behavior of AAFS. While HEDP·4Na has been extensively studied for its retardation effect in various cementitious systems, its influence on AAFS remains relatively unexplored. To comprehensively understand the effect of HEDP·4Na on the properties of AAFS, both workability and compressive strength were evaluated. Moreover, the microstructure and phase characteristic changes in AAFS paste with HEDP·4Na were also analyzed using TAM-air, scanning electron microscopy (SEM), thermogram analysis, and X-ray diffraction (XRD) techniques. By analyzing changes in microstructure and phase characteristics induced by HEDP·4Na, this research seeks to elucidate the mechanism underlying its retarding effect in the AAFS system. Such insights will contribute to optimizing the fresh properties of AAFS, advancing its practical utility in construction applications.

2. Experimental Program

2.1. Raw Materials

In this study, ground granulated blast-furnace slag (GGBS) and FA (Fly ash-I level) were used as precursors. The chemical compositions and particle size distribution of both materials are shown in Table 1 and Figure 1, respectively. In addition, the mineral composition of GGBS and FA was determined by X-ray diffraction (XRD), with the result presented in Figure 2. The alkaline activator commonly encompassed a combination of the sodium silicate liquid and sodium hydroxide solution (SHS). The modulus n was calculated as 3.34 based on the molar ratio of $[SiO_2]/[Na_2O]$ of sodium silicate liquid, consisting of 28.8 wt%SiO_2, 8.9 wt%Na_2O, and 62.3 wt%H_2O. This sodium silicate liquid is a commercial sodium water glass with a density of 1.384 g/cm^3 (CAS 1344-09-8). The prepared SHS was obtained by mixing sodium hydroxide (SH) solid powder (17.35 wt%, >96% purity) with de-ionized water, and the glass modulus of n was adjusted accordingly. It is worth noting that the SHS should be allowed to stand still for at least one day before being used to prepare AAFS paste.

Table 1. Chemical composition of GGBS and FA with X-ray fluorescence (%).

	CaO	SiO_2	Al_2O_3	MgO	SO_3	K_2O	Na_2O	Fe_2O_3	TiO_2	P_2O_5	LOI *
GGBS (%)	39.81	31.86	16.53	6.89	0.04	0.54	0.33	0.43	1.23	-	0.21
FA (%)	6.66	42.34	25.84	1.17	0.95	1.05	1.13	5.46	1.07	0.38	3.79

* Loss of ignition (1000 °C).

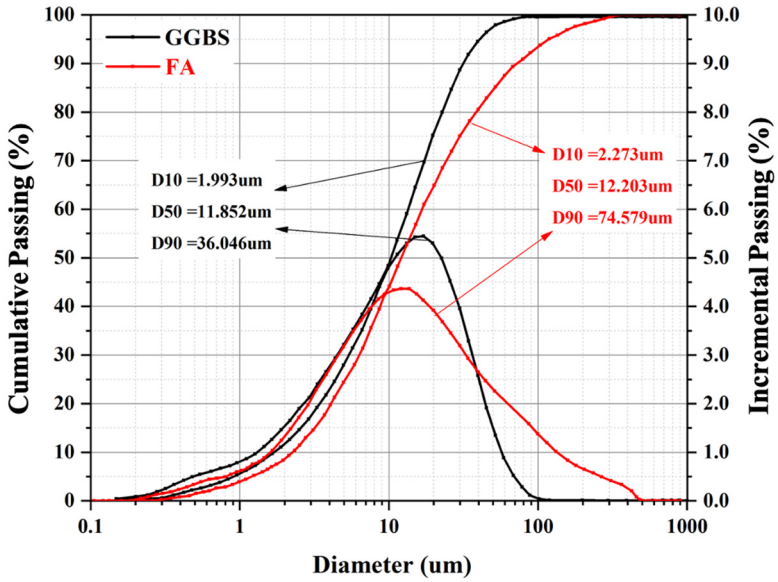

Figure 1. The particle size distribution of GGBS and FA.

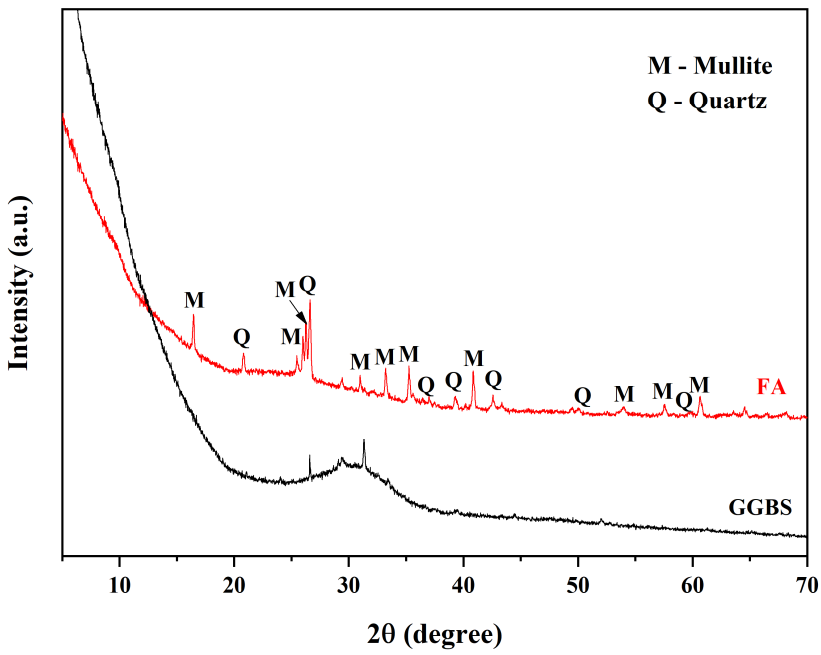

Figure 2. Mineral composition of GGBS and FA.

Green and low-cost HEDP·4Na solid powder served as an admixture in this study. The chemical structure of HEDP·4Na is depicted in Figure 3. Before mixing with other materials, the solid HEDP·4Na powder was dissolved in de-ionized water to ensure uniform distribution throughout the fresh paste. This process effectively enhances the properties of the alkaline activator liquid (AAL), aiming to meet standard performance crite-

ria, including workability, setting time, and compressive strength, as outlined in the BSI Standards [41–43].

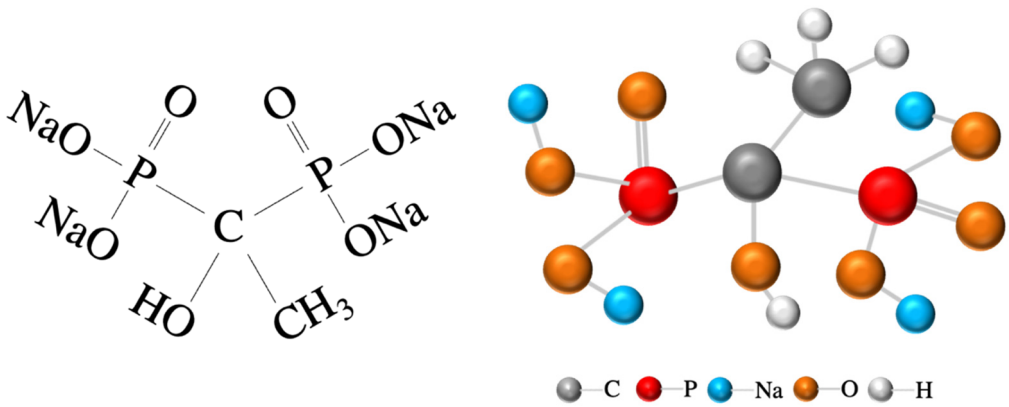

Figure 3. Schematic of the molecular structure of HEDP·4Na.

2.2. Mixture Proportion and Specimen Preparation

In this study, AAFS paste mixtures were proportioned to evaluate the influence of varying HEDP·4Na content on microstructure and microcosmic mechanisms. The influence of different mass ratios of GGBS and FA in alkali-activated material paste was examined. Previous studies have shown that the microstructure and shrinkage behaviors of alkali-activated paste are not significantly affected by mixtures that do not have a 50%-to-50% ratio of GGBS to FA [2,44–46]. Therefore, AAMs with a mass ratio of 1:1 for GGBS and FA in alkali-activated binders were selected for this investigation. The equivalent sodium oxide (Na_2O) content in the mixed activators used was 6% by mass of the binders. The water-to-binders ratio in all the prepared samples was 0.5, while the water-to-solid ratio was approximately 0.454, when considering the Na_2O and SiO_2 from the activators as parts of the solid. Additionally, the masses of HEDP·4Na added were 0.1%, 0.2%, and 0.3% of those of the binder materials, respectively. The mixture proportions of the AAFS paste are shown in Table 2.

Table 2. Mixture proportions of AAFS paste.

Mixture	GGBS (kg/m^3)	FA (kg/m^3)	NaOH (kg/m^3)	Na_2SiO_3 (kg/m^3)	Water (kg/m^3)	HEDP·4Na (Mass%)
P-0.0% HEDP·4Na	500	500	214.94	53.73	500	0
P-0.1% HEDP·4Na	500	500	214.94	53.73	500	0.1
P-0.2% HEDP·4Na	500	500	214.94	53.73	500	0.2
P-0.3% HEDP·4Na	500	500	214.94	53.73	500	0.3

To ensure the homogeneity of the HEDP·4Na solution, it was pre-mixed with AAL before being added to the solid precursors. The mixing process for the AAFS paste commenced with the dry mixing of the solid materials for 2 min, followed by the addition of the pre-mixed solution and further mixing for 3 min. Subsequently, the fresh paste was poured into cube steel molds of 20 × 20 × 20 mm^3 [47–49]. The molds were then vibrated on a vibrating table for 1 min and sealed with plastic sheets on the surface of all specimens for 24 h at room temperature. Finally, all specimens were demolded and placed in a standard curing room (20 ± 2 °C, 95% RH) until they reached the required curing testing ages.

2.3. Testing Methods

2.3.1. Setting Time and Workability

The initial and final setting times were determined using Vicat needle apparatus according to ASTM C191-18 [50], keeping the experimental atmosphere at 23 ± 3 °C. The initial setting time was defined as the duration between the initial contact of AAFS (or

cement) and AAL (or water) and the penetration of 25 mm. Similarly, the Vicat final time of setting was determined as the elapsed time between the initial contact of AAFS and AAL and the endpoint determination, which did not leave a complete circular impression on the specimen surface. The workability of paste specimens was assessed using a mini-slump cone [51], with dimensions of 20 mm for the top diameter, 40 mm for the bottom diameter, and 54 mm in height. To measure the flow spread of the fresh mixtures, the mini-slump cone was filled, and the flow spread was observed for 30 s in two perpendicular directions. The average value of these two measurements was recorded as the slump flow.

2.3.2. Mechanical Properties

Investigating the impact of varying HEDP·4Na concentrations on the mechanical performance of alkali-activated pastes, the compressive strength of the specimens (20 mm× 20 mm × 20 mm) was measured at specific curing ages under compression, with a loading rate of 0.42 kN/s. The compressive strength values were averaged from the three specimens.

2.3.3. Test Procedure

After the compressive strength test, all paste samples from each curing age were sectioned into several blocks and ground into powder. These blocks and powders were then dried in a vacuum oven at 60 °C for 24 h. Subsequently, microstructure and chemical analyses were conducted on all alkali-activated paste specimens using material characterization techniques, as described below:

- X-ray diffraction (XRD) analysis was conducted using a D8 Advance X-ray diffractometer (Bruker, Germany) with Cu Ka radiation (k = 1.5406 Å). The instrument was operated at a voltage of 40 KV and a current of 40 mA. Scans were performed in the 2θ range of 5° to 70° with a step of 0.02° to analyze the amorphous phase of AAFS paste powders.
- Isothermal calorimetry was performed on AAFS pastes using a TAM Air calorimeter (TA Instruments Co., New Castle, DE, USA) to assess the impact of HEDP·4Na on paste hydration. Paste samples were prepared using the external mixing method at a water-to-binder (w/b) ratio of 0.5. The solid mixtures of AAFS and the mixing liquid (AAL and water) were uniformly mixed with varying amounts (0%, 0.1%, 0.2%, and 0.3%) of HEDP·4Na in advance at a temperature of 20 °C.
- Differential thermal analysis (DTA) was performed using an STA8000 instrument (PerkinElmer Diamond, Waltham, MA, USA) to analyze the samples. Approximately 20 mg of dried powder from each prepared sample was placed into an alumina crucible, and the temperature was ramped from 30 °C to nearly 1000 °C at a heating rate of 10 °C/min. Fourier transform infrared spectroscopy (FTIR) was conducted using a Spectrum 100 instrument (PerkinElmer, Waltham, MA, USA) to identify hydration products via the KBr pellet technique. The spectra were obtained in the range of 4000 to 400 cm^{-1} at a resolution of 4 cm^{-1}.
- Microstructural morphological changes in the AAFS samples were analyzed using a scanning electron microscope (SEM, FEI, Quanta 250 FEG) equipped with energy-dispersive X-ray (EDX) analyzer. The samples were coated with gold using a K550X vacuum coater before testing.

3. Results and Discussion

3.1. TAM-Air

The calorimetric heat release curves of the alkali-activated pastes are illustrated in Figure 4. All alkali-activated pastes exhibited two characteristic peaks in the heat flow curves. The initial peak was observed within the first few minutes of the reaction, corresponding to the wetting and partial dissolution of solid materials, including FA, GGBS, and HEDP·4Na powder. The second peak, observed between 4.5 h and 14 h, indicates the formation of reaction products, potentially including the formation of calcium–HEDP

precipitates. This finding was also reported in [52]. The chelating properties of HEDP·4Na may affect the dissolution, precipitation, or stabilization of alkali-activated paste phases.

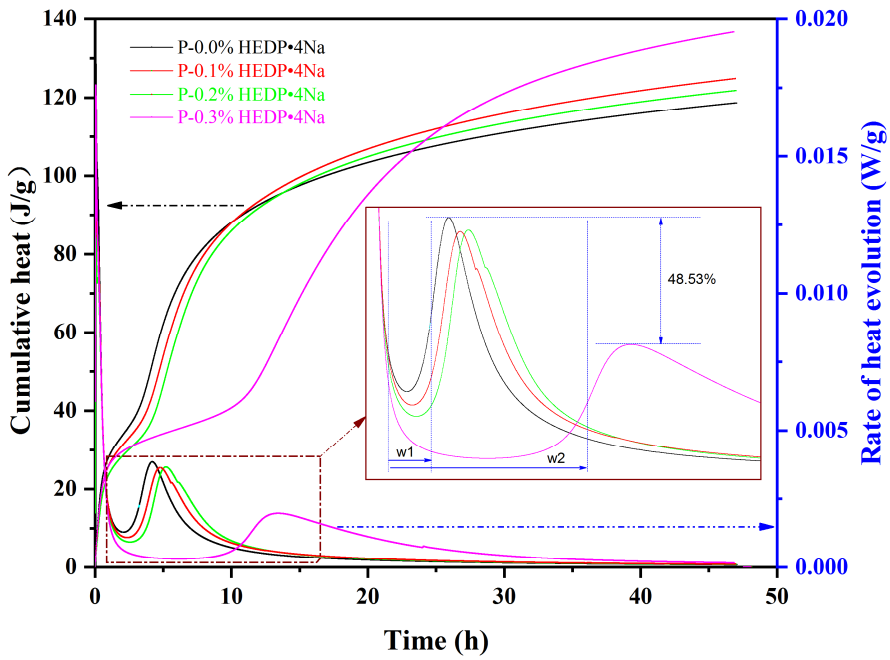

Figure 4. Hydration curves of AAM with different contents of HEDP·4Na.

To explore the influences of HEDP·4Na content on the reaction kinetics of alkali-activated mixtures, six indexes associated with hydration kinetics, including t_A, $(dQ/dt)_A$, Q_A, $K_{A\text{-}B}$, $(dQ/dt)_C$, and $Q_{A\text{-}C}$, were calculated based on the literature [53]. The calculated results of the six indexes are shown in Table 3. Compared to the AAFS mixture made without HEDP·4Na, the time required for t_A was delayed by 49%, 28%, and 400% when the AAFS mixtures contained 0.1%, 0.2%, and 0.3% of HEDP·4Na, respectively. Correspondingly, the rate of heat production during the dormant phase was reduced by 28%, 13%, and 76%, respectively. However, the cumulative heat flow at the beginning of the acceleration phase increased by 4% for the paste with 0.3% HEDP·4Na compared to the control group (P-0.0% HEDP·4Na). The chelating reaction of HEDP·4Na with metal ions from the alkali-activated paste mixtures may impact the kinetics of the alkaline activation process, which could potentially affect the development of compressive strength. The chemical reactions of AAFS paste were affected by this alkaline environment. Although HEDP·4Na can interact with different metal ions, such as calcium, magnesium, and iron, its ability to form complexes with aluminum ions may be limited due to the specific conditions of the alkaline-activated system. Under high-pH conditions, aluminum tended to form complex hydroxide species. In addition, research conducted by Gong et al. [54] suggested that the adsorption of HEDP·4Na was stronger on the surface of calcite than on the surface of brucite. At the same time, the calcium ion concentration was higher than that of other metal ions in this system (see Table 3). The possible chemical reactions of HEDP·4Na with metal ions in the system are shown as follows:

$$Ca^{2+} + HEDP^{4-} \rightleftharpoons CaHEDP^{2-} + 2OH^- \quad (1)$$

$$Fe^{2+} + HEDP^{4-} \rightleftharpoons FeHEDP^{2-} + 2OH^- \quad (2)$$

$$Fe^{3+} + HEDP^{4-} \rightleftharpoons FeHEDP^- + OH^- \quad (3)$$

$$Mg^{2+} + HEDP^{4-} \rightleftharpoons MgHEDP^- + 2OH^- \quad (4)$$

Table 3. Parameters of AAFS hydration extracted from the calorimetry curves of blank AAFS paste and the AAFS paste containing HEDP·4Na.

Items	t_A (h)	$(dQ/dt)_A$ (W/g)	Q_A (J/g)	K_{A-B} (W/(g·h))	$(dQ/dt)_C$ (W/g)	Q_{A-C} (J/g)
P-0.0% HEDP·4Na	2.0772	0.0013	33.9857	0.0010	0.0038	17.8139
P-0.1% HEDP·4Na	2.5659	0.0010	30.2868	0.0011	0.0037	18.6591
P-0.2% HEDP·4Na	2.3535	0.0011	32.5221	0.0006	0.0036	18.5391
P-0.3% HEDP·4Na	6.1659	0.0003	35.4217	0.0002	0.0020	21.9351

Note: t_A: the endpoint of the dormant phase; $(dQ/dt)_A$: the heat generation rate during the dormant phase; Q_A: the cumulative heat flow at the onset of the acceleration phase; K_{A-B}: the secant slope on the heat evolution curve between a and b; $(dQ/dt)_C$: the peak hydration rate observed in the acceleration; Q_{A-C}: the cumulative heat flow throughout the acceleration phase.

It should be noted that under specific conditions and concentrations, the stoichiometry and equilibrium constants of these reactions may vary, especially for the calcium-based phosphonate complex. For instance, two productions between calcium and HEDP could possibly be formed, including soluble HEDP-Ca complexes or Ca/HEDP precipitate [36]. Similarly, reactions might occur between calcium and HEDP·4Na.

During the acceleration period, the maximum hydration rates for the pastes with HEDP·4Na were lower than that of the paste without HEDP·4Na. This indicates a slowing down of alkaline-activated reaction rates due to the addition of HEDP·4Na. However, the amount of cumulative heat (Q_{A-C}) generated by the AAFS paste increased with the increase in HEDP·4Na content. This suggests the formation of a significant amount of C-(A)-S-H gel hydrates and chelating products of HEDP with metal ions in the system [55], which influence the strength development of alkali-activated pastes. This conclusion implies that the reactions with HEDP·4Na generated more heat than those without it. The increase in heat production may have resulted from chemical interactions or the influence of HEDP·4Na on reaction kinetics. Further investigation and analysis may be required to fully comprehend the role of HEDP·4Na in heat production during these reactions.

3.2. Workability and Setting Time of AAFS Mixture

Due to the chelation of the HEDP·4Na molecule with two phosphate groups and the calcium cation from the solution, the rate of dissolution of solid particles in the solution was prolonged, as evidenced by the extension of the induction period in Figure 4. As a result, the rate of the hydration reaction was decelerated, leading to an increase in both the workability and setting time for the AAFS paste containing HEDP·4Na.

The results of the mini-slump spread diameter of the AAFS mixtures are illustrated in Figure 5. The mini-slump flow increased with the increase in HEDP·4Na content. For instance, the mini slump of the AAFS mixture made with HEDP·4Na improved by 24% compared to the plain AAFS mixture. Due to the introduction of HEDP·4Na, there was a rise in the requirement for calcium cations in the alkali-activated paste to attain the same level of performance as the control sample without HEDP·4Na. While the liquid-to-binder ratio and FA-to-GGBS ratio were fixed in this study, competition for calcium ion demand between the HEDP·4Na molecule and alkaline activator was formed in an alkaline environment. Consequently, the spread diameter decreased for the paste without HEDP·4Na due to the deceleration in the rate of the reaction.

Figure 6 shows the initial and final setting times of the alkali-activated pastes made with various HEDP·4Na contents. The hardening process, which occurred without the significant development of compressive strength, lasted from 60 to 88 min. The setting time of the alkali-activated pastes was noticeably affected by the HEDP·4Na content. The increase in HEDP·4Na content from 0.0% to 0.3% led to both the initial and final setting time being delayed. However, the final setting times of all AAFS mixtures were less than 90 min.

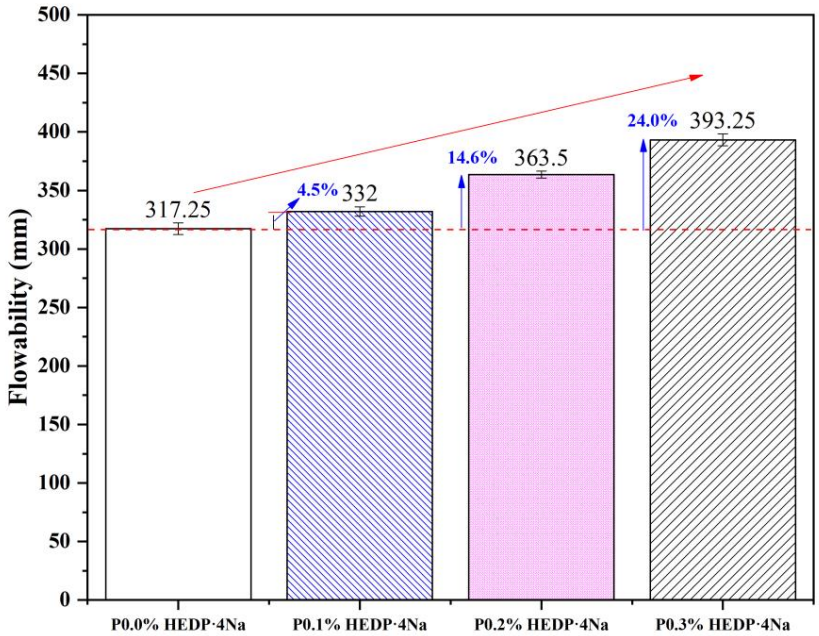

Figure 5. The mini slump of AAFS pastes with different HEDP·4Na contents.

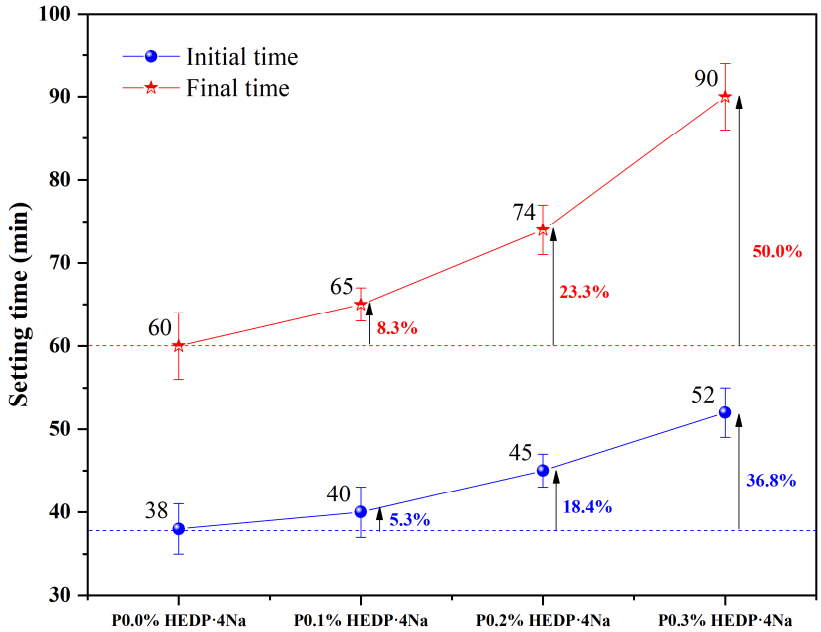

Figure 6. Influence of HEDP·4Na on initial and final setting times of AAFS paste.

3.3. Compressive Strength of AAFS

Figure 7 demonstrates the influence of HEDP·4Na content on the 7-, 14-, and 28-day compressive strength of the AAFS samples. The compressive strength was improved with the increase in HEDP·4Na content regardless of curing age. Compared to pastes without the addition in HEDP·4Na, those containing 0.1%, 0.2%, and 0.3% of HEDP·4Na exhibited 7-day compressive strength increases of 9.1%, 13.6%, and 15.9%, respectively. After 28 days of curing, pastes with corresponding HEDP·4Na contents showed incremental increases in compressive strength of 13.5%, 14.9%, and 16.2%, respectively, exceeding 40MPa. These findings suggest that the incorporation of HEDP·4Na effectively enhances the hydration degree of alkaline activator reactions, leading to the formation of C-S-H, C-A-S-H, and N-A-S-H, and/or a better spatial distribution of these hydration products [39]. During the induction period, the dissolution of calcium (Ca^{2+}), silica (Si^{4+}), and alumina (Al^{3+}) phases

in the alkaline environment was significantly influenced by the addition of HEDP·4Na. Subsequently, the formation of hydrated products contributed to the improved compressive strength of the alkaline-activated mixture.

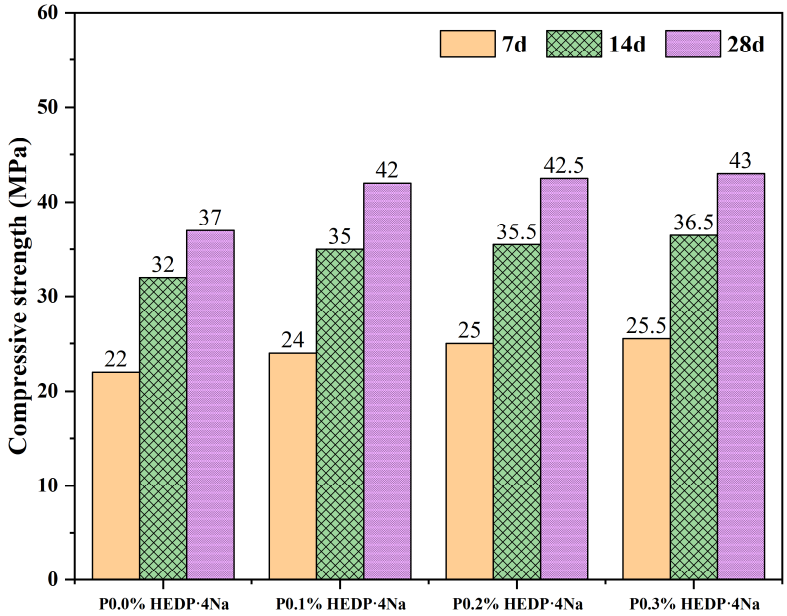

Figure 7. The compressive strength of all pastes at specific curing ages.

3.4. XRD Analysis

The results of the XRD analysis of the in situ binders (FA and GGBS) is shown in Figure 8. The main diffractograms of FA revealed quartz (Q) and mullite (M). A broad feature, often referred to as an 'amorphous hump', was observed between 20 and 35° (2θ), and it was associated with the glassy component present in the FA [56]. The diffraction patterns of the raw GGBS showed small detectable quantities of crystalline calcite and gypsum, alongside a predominantly amorphous material. The crystalline phase of trisodium phosphonoformate hexahydrate was detected in the raw HEDP·4Na material.

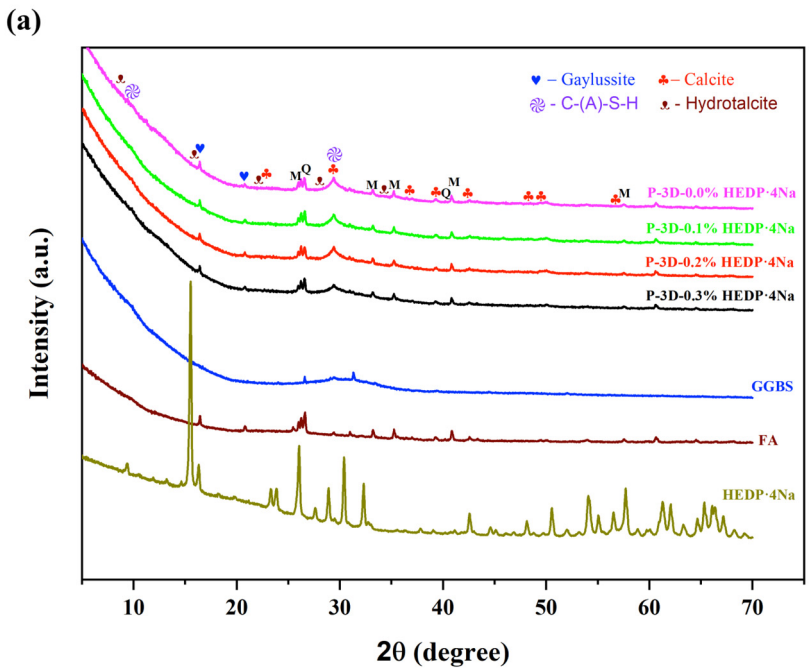

Figure 8. *Cont.*

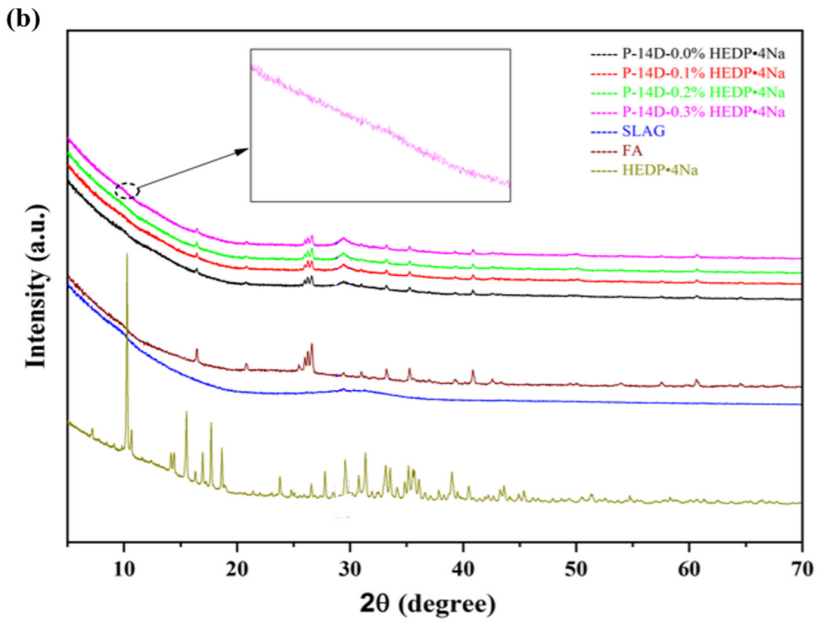

Figure 8. XRD patterns of AAFS mixtures at: (**a**) 3 days, (**b**) 14 days.

Mineralogical phases from unreacted FA, such as quartz and mullite, were observed in the diffraction curves of all alkaline-activated pastes at different curing ages, as shown in Figure 8. The reaction between FA/GGBS and the alkaline activator led to the formation of partially crystalline phases from amorphous phases. The main hydrated phases detected by XRD included a poorly crystalline C-(A)-S-H phase and a low-intensity peak of hydrotalcite (HT), formed through the alkaline activation of slags [57,58]. Calcite was detectable in the testing samples as well. With the incorporation of HEDP·4Na content, slight variations in the hydration products at different stages of the curing process were observed. The retarding formation of crystallinity was significantly influenced by the addition of HEDP·4Na, which was also verified by a calorimetry test. Similar phenomena have been reported in the literature [59,60]. Amorphous phases constitute the majority of AAFS reaction products, making it difficult to quantify C-A-S-H and N-A-S-(H) content individually. However, their content and distribution in the AAFS system were related to the properties of AAFS.

3.5. Thermogravimetric Analysis (TGA)

Figure 9 displays the TGA results for AAFS paste at 28 days. The mass loss during the measurement period was evaluated within the temperature range of 30–1000 °C, varying between 22% and 24%. The AAFS mixture made with 0.3% HEDP·4Na in total weight loss showed the highest mass loss compared to the other AAFS mixtures. A significant amount of weight loss can be observed at temperatures up to 300 °C due to the evaporation of water. Specifically, the mass loss percentages for the AAFS pastes, containing HEDP·4Na in concentrations ranging from 0.0% to 0.3%, were 13.5%, 13%, 12.5%, and 14.5%, respectively. This was because the water molecule is weakly bonded and escapes from the sample during this initial phase (between 30 and 100 °C). The material structure started to deteriorate due to the shrinkage of AAFS paste beyond this temperature, and mass loss was caused by the non-structurally bonded water in C-S-H or (C-A-S-H) in the second phase (from 100–300 °C) [55,61]. It can be observed that the mass loss of AAFS pastes with the addition of HEDP·4Na was slightly higher than that of the paste without HEDP·4Na, corresponding to the greater formation of hydration products. A precipitated Ca-phosphonate nanoparticle seeding effect and a more homogeneous hydration process may be also responsible for this [39]. When temperatures rose above 300 °C, the hydroxy groups began to dihydroxylate slowly. Relative dimensional stability was apparent in the material after removing most of the water. After being heated to 1000 °C, the mass loss corresponded to the decarbonization

of the carbonate phase. In the future, the use of HEDP·4Na may have a beneficial influence on the properties of AAFS paste.

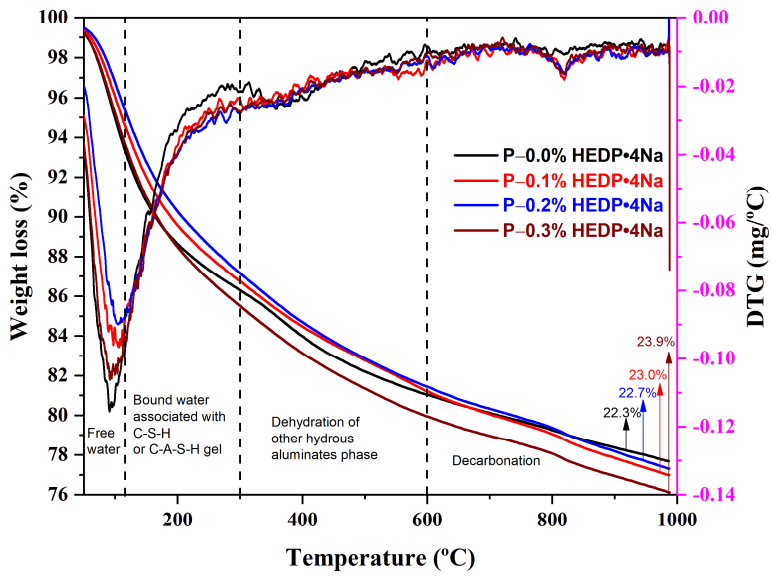

Figure 9. TGA analysis of AAFS pastes with different HEDP·4Na contents at 28 d.

3.6. SEM Analysis

The morphological characteristics of four AAFS paste specimens were examined using SEM operating at a voltage of 20 kV and a magnification of 8000×. The specimens, cured for 3 days, underwent vacuum drying for 12 h at 50 °C before testing.

At the early stage, the dissolution reaction mechanism occurs when the AAL dissolves some of the outer shells of the FA and GGBS particles in the process. This process leads to the leaching of Si-O-Al materials, which then form a cross-linked polyhedral polymer [62]. As observed in Figure 10, this polymer establishes a stable and three-dimensional structure. The unreacted and partially reacted FA particles can be seen in Figure 10. The reason was that smaller FA particles are more activated than larger ones. Activation and consumption were easier for finer particles than for coarser particles, which may be due to their easier absorption and more efficient conversion [63]. In contrast to FA, GGBS particles were solubilized during the alkaline activation, which was attributed to their higher vitreous phase content [63,64]. When the solubilization of FA and GGBS particles is poor, it might cause an insufficient amount of gel formation. Furthermore, it hinders the development of the compressive strength of AAFS paste [65]. Figure 10 demonstrates that the addition of HEDP·4Na leads to a denser microstructure in the AAFS matrix compared to samples without its addition. This may be attributed to its retardation effect and the influence of phosphonate on the degree of crystallinity. The use of HEDP·4Na was also elucidated to enhance the compressive strength of AAFS paste.

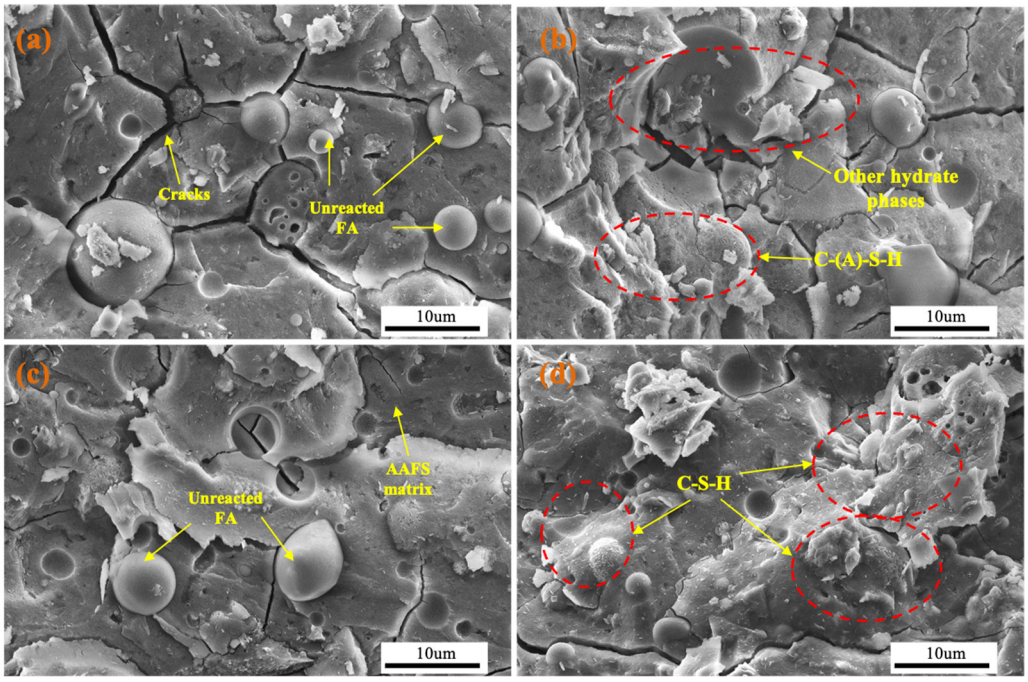

Figure 10. SEM analysis of AAFS pastes with (**a**) 0.0% HEDP·4Na, (**b**) 0.1% HEDP·4Na, (**c**) 0.2% HEDP·4Na, and (**d**) 0.3% HEDP·4Na.

4. Conclusions

This study investigated the effects of HEDP.4Na on the performance of the AAFS system. The development of the microstructural and phase characteristics of AAFS made with different HEDP·4Na contents was investigated, and the workability and compressive strength were also evaluated. The following conclusions can be drawn.

- The use of HEDP·4Na in the AAFS system exhibited a potential retardation effect on the rate of alkaline-activated reactions. This effect was advantageous for the dissolution of FA and GGBS particles in the early stage, facilitating the exposure of the glassy phase from precursor materials to the alkaline environment. The AAFS paste made with 0.3% HEDP·4Na content experienced an extension of almost 6 h during the induction period. Consequently, this process led to more hydration products being formed at the later stage.
- In contrast to the AAFS mixture without HEDP·4Na, the flowability of the AAFS mixture containing 0.1%, 0.2%, and 0.3% of HEDP·4Na showed increments of 5%, 15%, and 24%, respectively. Similarly, the initial setting time was prolonged by 5%, 19%, and 37%, respectively. The final setting time was also delayed by 8%, 23%, and 50%, respectively. This observation potentially demonstrates the favorable influence of HEDP·4Na on the rheological characteristics of the AAFS fresh mixture.
- An improvement in compressive strength was achieved due to the addition of HEDP·4Na to the AAFS specimens. Compared to the specimen without HEDP·4Na, the compressive strength of AAFS specimens incorporating 0.1%, 0.2%, and 0.3% of HEDP·4Na at 28 d was enhanced by 13.5%, 14.9%, and 16.2%, respectively.
- Compared to the plain AAFS, the use of HEDP·4Na in AAFS can result in the improvement of gel phases formation, such as C-S-H, as shown in TGA, XRD, and SEM analysis. This resulted in a denser microstructure and higher compressive strength in the AAFS made with HEDP.4Na.

While this study provides valuable insights into the influence of HEDP·4Na content on the properties of AAFS, there are certain limitations to consider. Firstly, this investigation exclusively explored the influence of HEDP·4Na on AAFS without considering potential interactions with other additives or variations in the AAFS system. This aspect should be

investigated in depth to understand the comprehensive effects of HEDP·4Na in various formulations. Secondly, while short-term effects were evaluated, long-term durability and performance should be studied. Assessing long-term durability, including resistance to chemical attacks and freeze–thaw cycles, is crucial to ascertain the effectiveness and robustness of the HEDP·4Na-modified AAFS mixture. This will enhance our understanding of the underlying mechanisms and optimize the application of HEDP·4Na in alkali-activated materials for various engineering applications.

Author Contributions: Conceptualization, B.Z., J.Z., M.Z. and J.W.; methodology, B.Z., J.Z. and J.W.; validation, B.Z. and M.Z.; formal analysis, J.Z. and M.Z.; investigation, B.Z., M.Z. and J.W.; resources, B.Z. and J.W.; data curation, B.Z. and J.Z.; writing—original draft preparation, B.Z.; writing—review and editing, M.Z. and J.W.; funding acquisition, J.W. and M.Z. All authors have read and agreed to the published version of the manuscript.

Funding: This research was funded by Shanghai Rising-Star Program (grant number: 21YF1449300).

Data Availability Statement: The original contributions presented in this study are included in the article; further inquiries can be directed to the corresponding author.

Conflicts of Interest: The authors declare no conflicts of interest.

References

1. Shi, C.; Jiménez, A.F.; Palomo, A. New Cements for the 21st Century: The Pursuit of an Alternative to Portland Cement. *Cem. Concr. Res.* **2011**, *41*, 750–763. [CrossRef]
2. Puertas, F.; Martínez-Ramírez, S.; Alonso, S.; Vázquez, T. Alkali-Activated Fly Ash/Slag Cements: Strength Behaviour and Hydration Products. *Cem. Concr. Res.* **2000**, *30*, 1625–1632. [CrossRef]
3. Abdalqader, A.F.; Jin, F.; Al-Tabbaa, A. Development of Greener Alkali-Activated Cement: Utilisation of Sodium Carbonate for Activating Slag and Fly Ash Mixtures. *J. Clean. Prod.* **2016**, *113*, 66–75. [CrossRef]
4. Liu, J.; Wang, Z.; Xie, G.; Li, Z.; Fan, X.; Zhang, W.; Xing, F.; Tang, L.; Ren, J. Resource Utilization of Municipal Solid Waste Incineration Fly Ash—Cement and Alkali-Activated Cementitious Materials: A Review. *Sci. Total Environ.* **2022**, *852*, 158254. [CrossRef] [PubMed]
5. Ramachandran, V.S.; Lowery, M.S.; Wise, T.; Polomark, G.M. The Role of Phosphonates in the Hydration of Portland Cement. *Mater. Struct.* **1993**, *26*, 425–432. [CrossRef]
6. Gopalakrishna, B.; Dinakar, P. Life Cycle Assessment (LCA) and the Influence of Alkaline Activator Content on Mechanical and Microstructural Properties of Geopolymer Mortar. *J. Eng. Res.* 2024, *in press*. [CrossRef]
7. Somna, K.; Jaturapitakkul, C.; Kajitvichyanukul, P.; Chindaprasirt, P. NaOH-Activated Ground Fly Ash Geopolymer Cured at Ambient Temperature. *Fuel* **2011**, *90*, 2118–2124. [CrossRef]
8. Choi, S.; Lee, K.M. Influence of Na_2O Content and Ms (SiO_2/Na_2O) of Alkaline Activator on Workability and Setting of Alkali-Activated Slag Paste. *Materials* **2019**, *12*, 2072. [CrossRef] [PubMed]
9. Fang, S.; Lam, E.S.S.; Li, B.; Wu, B. Effect of Alkali Contents, Moduli and Curing Time on Engineering Properties of Alkali Activated Slag. *Constr. Build. Mater.* **2020**, *249*, 118799. [CrossRef]
10. Chindaprasirt, P.; De Silva, P.; Sagoe-Crentsil, K.; Hanjitsuwan, S. Effect of SiO_2 and Al_2O_3 on the Setting and Hardening of High Calcium Fly Ash-Based Geopolymer Systems. *J. Mater. Sci.* **2012**, *47*, 4876–4883. [CrossRef]
11. Rakngan, W.; Williamson, T.; Ferron, R.D.; Sant, G.; Juenger, M.C.G. Controlling Workability in Alkali-Activated Class C Fly Ash. *Constr. Build. Mater.* **2018**, *183*, 226–233. [CrossRef]
12. Luo, Y.; Li, S.H.; Klima, K.M.; Brouwers, H.J.H.; Yu, Q. Degradation Mechanism of Hybrid Fly Ash/Slag Based Geopolymers Exposed to Elevated Temperatures. *Cem. Concr. Res.* **2022**, *151*, 106649. [CrossRef]
13. Fang, G.; Wang, Q.; Zhang, M. Micromechanical Analysis of Interfacial Transition Zone in Alkali-Activated Fly Ash-Slag Concrete. *Cem. Concr. Compos.* **2021**, *119*, 103990. [CrossRef]
14. Ye, H.; Radlińska, A. Fly Ash-Slag Interaction during Alkaline Activation: Influence of Activators on Phase Assemblage and Microstructure Formation. *Constr. Build. Mater.* **2016**, *122*, 594–606. [CrossRef]
15. Roy, D.M.; Jiang, W.; Silsbee, M.R. Chloride Diffusion in Ordinary, Blended, and Alkali-Activated Cement Pastes and Its Relation to Other Properties. *Cem. Concr. Res.* **2000**, *30*, 1879–1884. [CrossRef]
16. Shang, J.; Dai, J.G.; Zhao, T.J.; Guo, S.Y.; Zhang, P.; Mu, B. Alternation of Traditional Cement Mortars Using Fly Ash-Based Geopolymer Mortars Modified by Slag. *J. Clean. Prod.* **2018**, *203*, 746–756. [CrossRef]
17. Lee, N.K.; Lee, H.K. Reactivity and Reaction Products of Alkali-Activated, Fly Ash/Slag Paste. *Constr. Build. Mater.* **2015**, *81*, 303–312. [CrossRef]
18. Vigneshkumar, A.; Christy, C.F.; Muthukannan, M.; Maheswaran, M.; Arunkumar, K.; Devi, R.K. Experimental Investigations on Fresh and Mechanical Properties of Fly Ash and Ground Granulated Blast Furnace Slag Self-Compacting Geopolymer Concrete. *Mater. Today Proc.* 2024, *in press*. [CrossRef]

19. Li, J.; Sun, Z.; Wang, L.; Yang, X.; Zhang, D.; Zhang, X.; Wang, M. Properties and Mechanism of High-Magnesium Nickel Slag-Fly Ash Based Geopolymer Activated by Phosphoric Acid. *Constr. Build. Mater.* **2022**, *345*, 128256. [CrossRef]
20. Bayraktar, O.Y.; Bozkurt, T.H.; Benli, A.; Koksal, F.; Türkoğlu, M.; Kaplan, G. Sustainable One-Part Alkali Activated Slag/Fly Ash Geo-SIFCOM Containing Recycled Sands: Mechanical, Flexural, Durability and Microstructural Properties. *Sustain. Chem. Pharm.* **2023**, *36*, 101319. [CrossRef]
21. Raj, S.; Ramamurthy, K. Physical, Hydrolytic, and Mechanical Stability of Alkali-Activated Fly Ash-Slag Foam Concrete. *Cem. Concr. Compos.* **2023**, *142*, 105223. [CrossRef]
22. Wei, J.; Liu, J.; Khayat, K.H.; Long, W.J. Synergistic Effect of HEDP.4Na and Different Induced Pouring Angles on Mechanical Properties of Fiber-Reinforced Alkali-Activated Slag Composites. *Fibers* **2023**, *11*, 23. [CrossRef]
23. Ke, X.; Duan, Y. Coupling Machine Learning with Thermodynamic Modelling to Develop a Composition-Property Model for Alkali-Activated Materials. *Compos. Part B Eng.* **2021**, *216*, 108801. [CrossRef]
24. Antonić, T.; Čizmek, A.; Kosanović, C.; Subotić, B. Dissolution of Amorphous Aluminosilicate Zeolite Precursors in Alkaline Solutions. Part 1.—Kinetics of the Dissolution. *J. Chem. Soc. Faraday Trans.* **1993**, *89*, 1817–1822. [CrossRef]
25. Hajimohammadi, A.; van Deventer, J.S.J. Dissolution Behaviour of Source Materials for Synthesis of Geopolymer Binders: A Kinetic Approach. *Int. J. Miner. Process* **2016**, *153*, 80–86. [CrossRef]
26. Liu, X.; Li, S.; Ding, Y.; Lu, Z.; Stephan, D.; Chen, Y.; Wang, Z.; Cui, S. Investigation on Admixtures Applied to Alkali-Activated Materials: A Review. *J. Build. Eng.* **2023**, *64*, 105694. [CrossRef]
27. Paul, E. Influence of Superplasticizer on Workability and Strength of Ambient Cured Alkali Activated Mortar. *Clean. Mater.* **2022**, *6*, 100152. [CrossRef]
28. Akhlaghi, O.; Aytas, T.; Tatli, B.; Sezer, D.; Hodaei, A.; Favier, A.; Scrivener, K.; Menceloglu, Y.Z.; Akbulut, O. Modified Poly(Carboxylate Ether)-Based Superplasticizer for Enhanced Flowability of Calcined Clay-Limestone-Gypsum Blended Portland Cement. *Cem. Concr. Res.* **2017**, *101*, 114–122. [CrossRef]
29. Belhadi, R.; Govin, A.; Grosseau, P. Influence of Polycarboxylate Superplasticizer, Citric Acid and Their Combination on the Hydration and Workability of Calcium Sulfoaluminate Cement. *Cem. Concr. Res.* **2021**, *147*, 106513. [CrossRef]
30. Criado, M.; Palomo, A.; Fernández-Jiménez, A.; Banfill, P.F.G. Alkali Activated Fly Ash: Effect of Admixtures on Paste Rheology. *Rheol. Acta* **2009**, *48*, 447–455. [CrossRef]
31. Nematollahi, B.; Sanjayan, J. Effect of Different Superplasticizers and Activator Combinations on Workability and Strength of Fly Ash Based Geopolymer. *Mater. Des.* **2014**, *57*, 667–672. [CrossRef]
32. Sasaki, K.; Kurumisawa, K.; Ibayashi, K. Effect of Retarders on Flow and Strength Development of Alkali-Activated Fly Ash/Blast Furnace Slag Composite. *Constr. Build. Mater.* **2019**, *216*, 337–346. [CrossRef]
33. Gledhill, W.E.; Feijtel, T.C.J. Environmental Properties and Safety Assessment of Organic Phosphonates Used for Detergent and Water Treatment Applications. *Detergents* **1992**, 261–285. [CrossRef] [PubMed]
34. Nowack, B. Environmental Chemistry of Phosphonates. *Water Res.* **2003**, *37*, 2533–2546. [CrossRef]
35. Zeng, B.; Li, M.D.; Zhu, Z.P.; Zhao, J.M.; Zhang, H. Application of 1-Hydroxyethylidene-1, 1-Diphosphonic Acid in Boiler Water for Industrial Boilers. *Water Sci. Technol.* **2013**, *67*, 1544–1550. [CrossRef] [PubMed]
36. Browning, F.H.; Fogler, H.S. Effect of Precipitating Conditions on the Formation of Calcium−HEDP Precipitates. *Langmuir* **1996**, *12*, 5231–5238. [CrossRef]
37. Gu, P.; Ramachandran, V.S.; Beaudoin, J.J.; Quinn, E. Electrochemical Behavior of Portland Cement Pastes Containing Phosphonates. *Adv. Cem. Based Mater.* **1995**, *2*, 182–188. [CrossRef]
38. Lupu, C.; Arvidson, R.S.; Lüttge, A.; Barron, A.R. Phosphonate Mediated Surface Reaction and Reorganization: Implications for the Mechanism Controlling Cement Hydration Inhibition. *Chem. Commun.* **2005**, *18*, 2354–2356. [CrossRef] [PubMed]
39. Kiiashko, A.; Chaouche, M.; Frouin, L. Effect of Phosphonate Addition on Sodium Carbonate Activated Slag Properties. *Cem. Concr. Compos.* **2021**, *119*, 103986. [CrossRef]
40. Liang, H.; Liu, J.; Kang, B.; Zhang, Y.; He, Y.; Yang, H. Optimizing 1-Hydroxyethylidene-1,1-Diphosphonic Acid and Mechanically-Activated Iron Ore Tailings to Prepare Low-Cost and Retarded Magnesium Oxysulfate Cement. *Case Stud. Constr. Mater.* **2022**, *17*, e01631. [CrossRef]
41. BS EN 206:2013+A2:2021-Concrete-Specification, Performance, Production and Conformity. Available online: https://landingpage.bsigroup.com/LandingPage/Standard?UPI=000000000030407978 (accessed on 9 May 2024).
42. Junaid, M.T.; Kayali, O.; Khennane, A.; Black, J. A Mix Design Procedure for Low Calcium Alkali Activated Fly Ash-Based Concretes. *Constr. Build. Mater.* **2015**, *79*, 301–310. [CrossRef]
43. CEN-EN 197-1—Cement Part 1: Composition, Specifications and Conformity Criteria for Common Cements | GlobalSpec. Available online: https://standards.globalspec.com/std/1399038/EN%20197-1 (accessed on 31 January 2024).
44. Li, Z.; Lu, T.; Liang, X.; Dong, H.; Ye, G. Mechanisms of Autogenous Shrinkage of Alkali-Activated Slag and Fly Ash Pastes. *Cem. Concr. Res.* **2020**, *135*, 106107. [CrossRef]
45. Li, Z.; Nedeljkovic, M.; Zuo, Y.; Ye, G. Autogenous Shrinkage of Alkali-Activated Slagfly Ash Pastes. In Proceedings of the 5th International Slag Valorisation Symposium, Leuven, Belgium, 3–5 April 2018; pp. 369–372.
46. Huang, D.; Chen, P.; Peng, H.; Yuan, Q.; Tian, X. Drying Shrinkage Performance of Medium-Ca Alkali-Activated Fly Ash and Slag Pastes. *Cem. Concr. Compos.* **2022**, *130*, 104536. [CrossRef]

47. Mo, L.; Fang, J.; Huang, B.; Wang, A.; Deng, M. Combined Effects of Biochar and MgO Expansive Additive on the Autogenous Shrinkage, Internal Relative Humidity and Compressive Strength of Cement Pastes. *Constr. Build. Mater.* **2019**, *229*, 116877. [CrossRef]
48. Li, N.; Unluer, C. Development of High-Volume Steel Slag as Cementitious Material by Ethylenediamine Tetraacetic Acid Induced Accelerated Carbonation. *Powder Technol.* **2023**, *428*, 118899. [CrossRef]
49. Guettala, S.; Mezghiche, B. Compressive Strength and Hydration with Age of Cement Pastes Containing Dune Sand Powder. *Constr. Build. Mater.* **2011**, *25*, 1263–1269. [CrossRef]
50. *C 191-08*; Standard Test Methods for Time of Setting of Hydraulic Cement by Vicat Needle 1. ASTM International: West Conshohocken, PA, USA, 2021.
51. C1611/C1611M Standard Test Method for Slump Flow of Self-Consolidating Concrete. Available online: https://www.astm.org/c1611_c1611m-21.html (accessed on 31 January 2024).
52. Brough, A.R.; Atkinson, A. Sodium Silicate-Based, Alkali-Activated Slag Mortars: Part I. Strength, Hydration and Microstructure. *Cem. Concr. Res.* **2002**, *32*, 865–879. [CrossRef]
53. Zhang, Y.R.; Kong, X.M.; Lu, Z.B.; Lu, Z.C.; Hou, S.S. Effects of the Charge Characteristics of Polycarboxylate Superplasticizers on the Adsorption and the Retardation in Cement Pastes. *Cem. Concr. Res.* **2015**, *67*, 184–196. [CrossRef]
54. Gong, X.; Yao, J.; Yang, B.; Fu, Y.; Wang, Y.; Yin, W. Selective Flotation of Brucite from Calcite Using HEDP-4Na as an Inhibitor in a SDS System. *J. Ind. Eng. Chem.* **2023**, *125*, 390–401. [CrossRef]
55. Shi, C.; Roy, D.; Krivenko, P. *Alkali-Activated Cements and Concretes*; CRC Press: London, UK, 2003; p. 392.
56. Baraka-Lokmane, S.; Sorbie, K.S. Effect of PH and Scale Inhibitor Concentration on Phosphonate–Carbonate Interaction. *J. Pet. Sci. Eng.* **2010**, *70*, 10–27. [CrossRef]
57. Haha, M.B.; Lothenbach, B.; Le Saout, G.; Winnefeld, F. Influence of Slag Chemistry on the Hydration of Alkali-Activated Blast-Furnace Slag—Part I: Effect of MgO. *Cem. Concr. Res.* **2011**, *41*, 955–963. [CrossRef]
58. Oh, J.E.; Monteiro, P.J.M.; Jun, S.S.; Choi, S.; Clark, S.M. The Evolution of Strength and Crystalline Phases for Alkali-Activated Ground Blast Furnace Slag and Fly Ash-Based Geopolymers. *Cem. Concr. Res.* **2010**, *40*, 189–196. [CrossRef]
59. Peronno, D.; Cheap-Charpentier, H.; Horner, O.; Perrot, H. Study of the Inhibition Effect of Two Polymers on Calcium Carbonate Formation by Fast Controlled Precipitation Method and Quartz Crystal Microbalance. *J. Water Process Eng.* **2015**, *7*, 11–20. [CrossRef]
60. Trushina, D.B.; Bukreeva, T.V.; Kovalchuk, M.V.; Antipina, M.N. $CaCO_3$ Vaterite Microparticles for Biomedical and Personal Care Applications. *Mater. Sci. Eng. C* **2014**, *45*, 644–658. [CrossRef] [PubMed]
61. Collier, N.C. Transition and Decomposition Temperatures of Cement Phases—A Collection of Thermal Analysis Data. *Ceram. Silik.* **2016**, *60*, 338–343. [CrossRef]
62. Khater Hisham, M.; Elnagar Abdeen, M.; Ezzat, M. Optimization of Alkali ActivatedGrog/Ceramic Wastes Geopolymer Bricks. *Int. J. Innov. Res. Sci. Eng. Technol.* **2016**, *5*, 37–46.
63. Kumar, S.; Kumar, R.; Alex, T.C.; Bandopadhyay, A.; Mehrotra, S.P. Influence of Reactivity of Fly Ash on Geopolymerisation. *Adv. Appl. Ceram.* **2007**, *106*, 120–127. [CrossRef]
64. Fang, G.; Zhang, M. Multiscale Micromechanical Analysis of Alkali-Activated Fly Ash-Slag Paste. *Cem. Concr. Res.* **2020**, *135*, 106141. [CrossRef]
65. Gao, K.; Lin, K.L.; Wang, D.; Hwang, C.L.; Shiu, H.S.; Chang, Y.M.; Cheng, T.W. Effects SiO_2/Na_2O Molar Ratio on Mechanical Properties and the Microstructure of Nano-SiO_2 Metakaolin-Based Geopolymers. *Constr. Build. Mater.* **2014**, *53*, 503–510. [CrossRef]